processes

MDPI

Article

Fast and Efficient Removal of Uranium onto a Magnetic Hydroxyapatite Composite: Mechanism and Process Evaluation

Tao Ou [1,2], Hairong Peng [1,2], Minhua Su [1,2,*], Qingpu Shi [1,2], Jinfeng Tang [2,*], Nan Chen [1,2] and Diyun Chen [1,2]

[1] Guangdong Provincial Key Laboratory of Radionuclides Pollution Control and Resources, Guangzhou University, Guangzhou 510006, China; outao1997@163.com (T.O.); drogba11phr@foxmail.com (H.P.); L60882969@163.com (Q.S.); nancychen@gzhu.edu.cn (N.C.); cdy@gzhu.edu.cn (D.C.)

[2] School of Environmental Science and Engineering, Guangzhou University, Guangzhou 510006, China

* Correspondence: mhsu@gzhu.edu.cn (M.S.); jinfeng@gzhu.edu.cn (J.T.)

Abstract: The exploration and rational design of easily separable and highly efficient sorbents with satisfactory capability of extracting radioactive uranium (U)-containing compound(s) are of paramount significance. In this study, a novel magnetic hydroxyapatite (HAP) composite (HAP@$CoFe_2O_4$), which was coupled with cobalt ferrite ($CoFe_2O_4$), was rationally designed for uranium(VI) removal through a facile hydrothermal process. The U(VI) ions were rapidly removed using HAP@$CoFe_2O_4$ within a short time (i.e., 10 min), and a maximum U(VI) removal efficiency of 93.7% was achieved. The maximum adsorption capacity (Q_{max}) of the HAP@$CoFe_2O_4$ was 338 mg/g, which demonstrated the potential of as-prepared HAP@$CoFe_2O_4$ in the purification of U(VI) ions from nuclear effluents. Autunite [$Ca(UO_2)_2(PO_4)_2(H_2O)_6$] was the main crystalline phase to retain uranium, wherein U(VI) was effectively extracted and immobilized in terms of a relatively stable mineral. Furthermore, the reacted HAP@$CoFe_2O_4$ can be magnetically recycled. The results of this study reveal that the suggested process using HAP@$CoFe_2O_4$ is a promising approach for the removal and immobilization of U(VI) released from nuclear effluents.

Keywords: cobalt ferrite; adsorption; hydroxyapatite; mineralization; uranium(VI)

Citation: Ou, T.; Peng, H.; Su, M.; Shi, Q.; Tang, J.; Chen, N.; Chen, D. Fast and Efficient Removal of Uranium onto a Magnetic Hydroxyapatite Composite: Mechanism and Process Evaluation. *Processes* **2021**, *9*, 1927. https://doi.org/10.3390/pr9111927

Academic Editor: Andrea Petrella

Received: 19 September 2021
Accepted: 21 October 2021
Published: 28 October 2021

1. Introduction

Uranium (U), a long-persisting and highly hazardous radionuclide, is generally released from uranium mining, nuclear weapon testing, and nuclear accidents. Uranium released from untreated wastewater poses serious threats to aquatic life and human health [1–4]. Because of the high mobility of uranium(VI) ions under oxidizing conditions and the consequent environmental risks, the retardation and immobilization of UO_2^{2+}, which is the most stable uranium specie, have attracted considerable attention [5]. Adsorption is the most facile and promising approach to the treatment of metal ions because of its low cost, high efficiency, and ease of operation [6–10].

Many cost-effective and ecofriendly adsorbents with components ubiquitous in the environment have been fabricated to remove U(VI) or other heavy metal ions, including iron and manganese oxides or hydroxides, organic matter, silicates, phosphate minerals, clay minerals and their modified forms [11–17]. Hydroxyapatite [$Ca_{10}(PO_4)_6(OH)_2$, HAP] is a promising absorbent material because it can effectively immobilize considerable amounts of U(VI) due to its unique physical, chemical, mechanical, and biological properties [18,19]. Because UO_2^{2+} exhibits a strong affinity for PO_4^{3-}, and their product uranyl phosphate generally has low solubility under most conditions, the phosphate group in the HAP structure dominates the transport and transformation behavior of U(VI) in nature [5,20–22]. Autunite, meta-autunite, torbernite, meta-torbernite, and uranyl selenite are the principal uranyl minerals, and phosphorus can be used to promote the mineralization and retention of U(VI) to form stable secondary uranium minerals to mitigate U pollution in the environment [23]. Numerous studies have been performed on the morphology control, synthesis,

and adsorption applications of HAP. Zhou et al. [24] reported the synthesis of strontium (Sr) doped hydroxyapatite (HAP) for the increased Cr(VI) adsorption through a hydrothermal method. Ma et al. [25] found that the addition of a certain amount of alendronate in the synthesis of hydroxyapatite helped to form a loose porous nanospheres with low crystallinity, showing good adsorption capacity for Pb^{2+}, Cu^{2+}, and Cd^{2+}. Xiong et al. [26] and Su et al. [27] revealed that HAP with a porous structure can remove U(VI) ions from an aqueous solution. Although such HAP materials can remove pollutants, a key problem is the separation of granular absorbents. Therefore, the rational design of a fast, efficient, and easily separable emergency material is critical for the purification of U(VI)-containing wastewater from the nuclear industry or in case of accidents.

$CoFe_2O_4$, a compound with excellent magnetic and unique properties, has been widely used in applications, such as permanent magnets, storage devices, magnetic recording, electronics, and pigments [28–31]. Compared with Fe_3O_4, $CoFe_2O_4$ has more advantages, such as simpler synthesis, more hydroxyl groups on the surface, and excellent chemical inertness [32–35]. Many researchers have verified the potential of $CoFe_2O_4$ and its magnetic recovery [36–38]. To effectively recover the adsorbed material and maintain the stability of the target material, nano $CoFe_2O_4$ and HAP can be coupled through a facile hydrothermal process. The as-synthesized HAP@$CoFe_2O_4$ exhibits superior composition uniformity, narrow particle size distribution, and can be therefore magnetically separated from reaction systems [39]. To the best of our knowledge, the use of a rationally designed HAP@$CoFe_2O_4$ composite as a sorbent to abate and fix U(VI) has been rarely reported.

This study aims to (I) synthesize easily separable and highly efficient HAP@$CoFe_2O_4$ through a facile hydrothermal method, (II) investigate the interaction between HAP@$CoFe_2O_4$ and U(VI) ions, (III) determine the mechanisms toward U(VI) removal using magnetic HAP@$CoFe_2O_4$ and (IV) develop a preliminary process for the U(VI) removal. The U(VI) adsorption behavior by HAP@$CoFe_2O_4$ was discussed in detail based on the outcomes from equilibrium and kinetics analysis. The findings of this study provide a promising and economic material for the treatment of uranium-contaminated sites.

2. Materials and Methods

2.1. Materials

Citric acid ($C_6H_8O_7$, 99%) was obtained from Tianjin Fuchen Chemical Reagent Factory (Tianjin, China). Salts of calcium (II) ($Ca(NO_3)_2$, 99%), iron (III) ($FeCl_3 \cdot 6H_2O$, 99%), and cobalt (II) ($CoCl_2 \cdot 6H_2O$, 98%) were purchased from Tianjin Fuchen Chemical Reagent Factory (Tianjin, China) and Shanghai Aladdin Biochemical Technology Co., Ltd. (Shanghai, China). Both diammonium hydrogen phosphate ($(NH_4)_2HPO_4$) and aqua ammonia ($NH_3 \cdot H_2O$, 25–28%) were purchased from Sinopharm Chemical Reagent Co., Ltd. (Shanghai, China). Ethylene glycol ($(CH_2OH)_2$, $\geq$99.5%) were purchased from Shanghai Aladdin Biochemical Technology Co., Ltd. A stock solution containing 1 g/L of uranium was prepared by dissolving $UO_2(NO_3)_2 \cdot 6H_2O$ in ultrapure water.

2.2. Synthesis and Characterizations of HAP@$CoFe_2O_4$

Nanosized HAP that was used as a precursor was prepared using a chemical precipitation method described in our previous study [40]. The HAP@$CoFe_2O_4$ composite was hydrothermally fabricated (Text S1 in Supplementary Materials). The initial mole ratio of HAP/$CoFe_2O_4$ is 0.5/1. First, 30 mL of ethylene glycol and 20 mL of ultrapure water were added to the beaker, and subsequently, 0.5 mmol of HAP precursors were added to the beaker and sonicated for 15 min to ensure uniform dispersion. Then, 2 mmol of ferric chloride and 1 mmol of cobalt chloride were added to the beaker and stirred until they were dissolved. Aqua ammonia was titrated to increase the pH of the solution to 10.0 with magnetic stirring at room temperature for 1 h. The mixed solution was transferred into a 100 mL Teflon-lined, stainless-steel autoclave and stored at 180 °C for 24 h to facilitate reactions in an oven. Then, the autoclave was cooled to room temperature naturally, and the precipitates were obtained. The precipitates were centrifuged and washed with

alcohol and ultrapure water 3–4 times, and finally, the obtained solid was placed in a constant-temperature oven and dried at 60 °C for 4 h.

The prepared adsorbent samples' phases and crystal structures were determined through an X-ray diffraction (XRD) instrument with Cu K_α radiation (λ = 1.5418 Å) operated at a 2000 W power and 10°/min scanning rate in the 2θ range from 10° to 90°. Additionally, the specific surface area, magnetic properties, and functional groups of the as-prepared samples were analyzed using the Brunauer–Emmett–Teller specific surface analyzer (ASAP 2020, Micromeritics, Norcross, GA, USA), magnetometer (VSM, Dexing, Model: 250), and Bruker Tensor 27 FT-IR spectrometer (Bruker Tensor27, Germany), respectively. The surface morphology and elemental compositions of the HAP@$CoFe_2O_4$ samples were characterized by a transmission electron microscope (JEOLJSM-2100F, Japan) and X-ray photoelectron spectroscopy (Thermo Fisher Scientific ESCALAB250Xi spectrometer, Waltham, MA, USA). The point of zero charge (pzc) of the HAP@$CoFe_2O_4$ was measured by a Zeta potentiometer (NanoBrook Zeta PALS Potential Analyzer, Brookhaven Instruments, Holtsville, NY, USA).

2.3. U(VI) Removal Experiments

A series of batch sorption experiments were performed to investigate the U(VI) removal performance of HAP@$CoFe_2O_4$. The solution volume was 50 mL. The influence of pH was investigated in the range of 2.0–6.0. The dosage of the sorbent varied from 0.1 to 0.3 g/L. A dosage of 0.2 g/L of HAP@$CoFe_2O_4$ exhibited excellent U(VI) removal ability and was thus selected as the optimal dosage for the experiments, while the initial U(VI) concentration and contact time varied. The residual U in the solution after filtration was determined using a uranium microanalyzer. The amount of U(VI) ions adsorbed by the adsorbent at time t was estimated using Equation (1):

$$Q_t = \frac{(C_0 - C_t)V}{m} \quad (1)$$

In Equation (1), Q_t, C_0, C_t, V, and m denote the adsorption capacity of HAP@$CoFe_2O_4$ for U(VI) at time t, initial U(VI) concentration (mg/L), U(VI) concentration measured at time t, volume of the reaction system, and the adsorbent's mass, respectively.

3. Results and Discussion

3.1. Characterization

The X-ray diffraction (XRD) patterns of the HAP@$CoFe_2O_4$ are illustrated in Figure 1a. The diffraction characteristic peaks of the HAP@$CoFe_2O_4$ located at 25.338°, 31.740°, and 49.463° corresponded to the (201), (211), and (213) planes, respectively, of typical hydroxyapatite (PDF no. 09-0432). The characteristic peaks of the HAP@$CoFe_2O_4$ were located at 29.946°, 35.270°, 42.862°, 56.672°, and 65.422°, which corresponded to the planes of (220), (311), (400), (511), and (531) of $CoFe_2O_4$ (PDF no. 22-1086), respectively. The average microcrystalline size of the $CoFe_2O_4$ calculated by Scherer equation (Equation S1) is 10.60 nm. The HAP@$CoFe_2O_4$ almost preserved the crystal structure of the HAP during the preparation process. The XRD results indicated that a hybrid material composed of HAP and $CoFe_2O_4$ was obtained.

Figure 1b indicated that the HAP@$CoFe_2O_4$ exhibited a specific surface area of 12.161 m^2/g, which suggested that the as-obtained HAP@$CoFe_2O_4$ could be beneficial for interface reactions because of the sufficient active sites. The N_2 adsorption-desorption isotherm of HAP@$CoFe_2O_4$ was a type IV curve and belonged to the H3 type hysteresis loop, which indicated that HAP@$CoFe_2O_4$ is a flat slit structure. The average pore size of the product calculated according to the Barrett–Joyner–Halenda (BJH) method was 15.292 nm.

A broad peak near 3448.3 cm^{-1}, which can be attributed to the stretching vibration of the –OH groups, was observed in the Fourier-transform infrared (FT-IR) spectra of the HAP@$CoFe_2O_4$ (Figure 1c). This spectrum, which exhibited bands at 2360.99 cm^{-1} and

between 1476.14 and 1383.85 cm^{-1} could be explained by the adhesion of CO_2 from the atmosphere during the synthesis of the HAP in highly alkaline conditions [41–43]. The peak at 1638.06 cm^{-1} was related to the –COO group, possibly because of the citric acid added during synthesis. The peaks at approximately 572.89 and 602.94 cm^{-1} represented asymmetric bending vibration, and the peak at 1044.82 cm^{-1} represented symmetric stretching vibration; these were attributed to the tetrahedron PO_4^{3-} groups of HAP. For FT-IR, Co/Fe–O bonds are typical in the 580–598 banding [44–46]. In this case, the peak of the Co/Fe–O bond may have overlapped with the typical vibration of the PO_4^{3-} group of HAP. The charge on the surface of the material affects its adsorption performance. As displayed in Figure 1d, the pHpzc of the HAP@$CoFe_2O_4$ was approximately 2.8, even in the solution with 15 ppm U(VI).

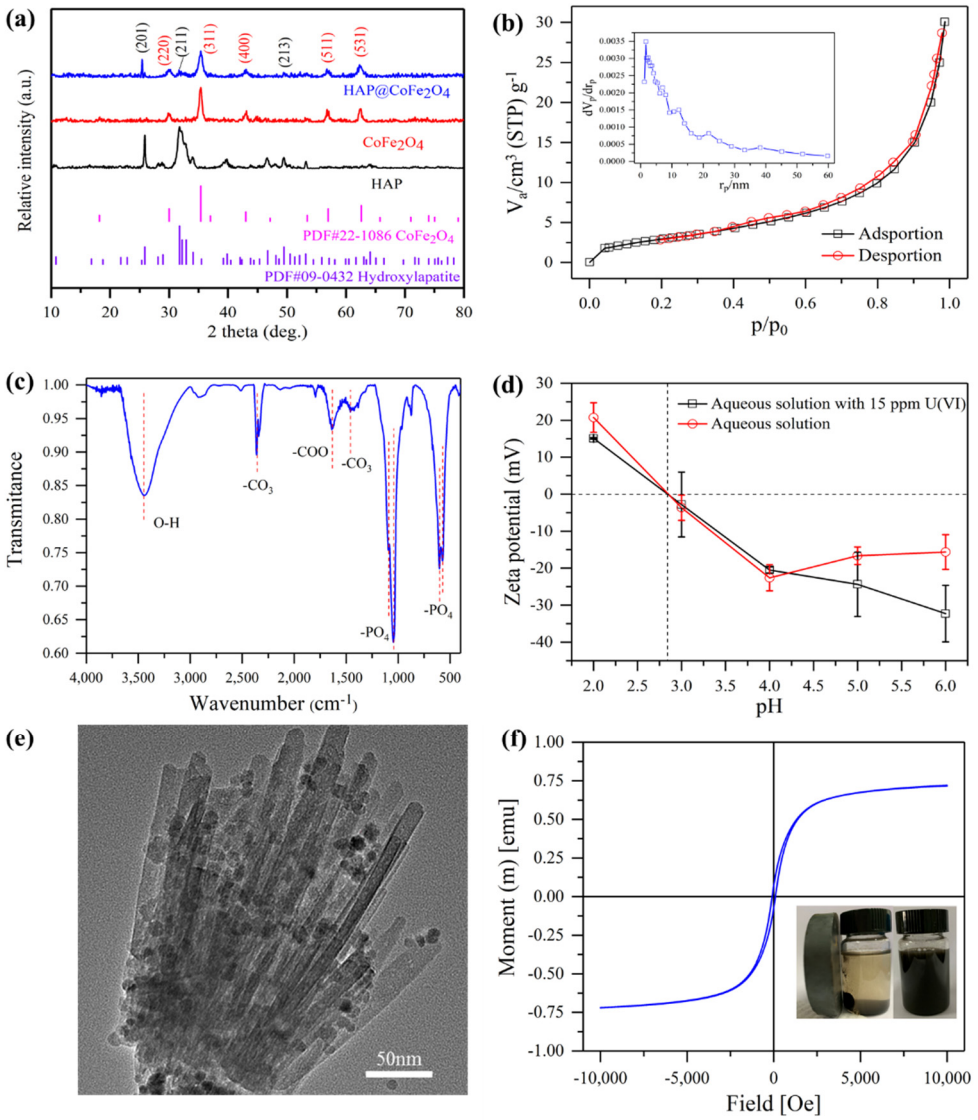

Figure 1. XRD patterns (**a**) of HAP, $CoFe_2O_4$ as well as HAP@$CoFe_2O_4$, (**b**) the nitrogen adsorption-desorption isotherm (calculated from the Brunauer–Emmett–Teller [BET method] and pore size distribution (calculated from the BJH method), (**c**) Fourier transform infrared [FT-IR] spectrum, (**d**) zeta-potential and (**e**) transmission electron microscopy (TEM) image, and (**f**) the hysteresis loop of HAP@$CoFe_2O_4$ (inset of Figure 1f displays the separation of HAP@$CoFe_2O_4$ with and without an additional magnet).

Because the morphology including size and shape of nanomaterials considerably affected the physical and chemical properties of the product, the morphology of the

HAP@$CoFe_2O_4$ was investigated through transmission electron microscopy (TEM). As presented in Figure 1e, HAP@$CoFe_2O_4$ morphology showed a typical bundle-like structure with numerous $CoFe_2O_4$ nanoparticles. $CoFe_2O_4$ was evenly dispersed and tightly adhered to the surface of the HAP. The results from hysteresis loop analysis showed that the as-prepared HAP@$CoFe_2O_4$ possessed excellent magnetic properties, suggesting that HAP@$CoFe_2O_4$ could be easily separated using an extra magnet within a short time after the reaction (Figure 1f). Compared with other separation technology (e.g., filtering and centrifugal separation) applying an external magnetic field and using magnetic material(s) allows the adsorbent to be more quickly recovered from the reaction system and thus saving time and cost. These results revealed that the HAP@$CoFe_2O_4$ composites were successfully synthesized and can be applied in the treatment process of eliminating U(VI) from the aqueous solution.

3.2. U(VI) Removal by Magnetic HAP@$CoFe_2O_4$

Dosage experiments were conducted for confirming the optimal dosage of adsorbents. As shown in Figure 2a, with an increase in the dosage, the adsorption sites increased in the solution, which were more conducive to the binding of UO_2^{2+}, leading to the improvement of removal efficiency. The HAP@$CoFe_2O_4$ maintained the high efficiency adsorption of U(VI). The HAP considerably dominated the adsorption process, whereas the adsorption contribution of the $CoFe_2O_4$ to U(VI) was insignificant.

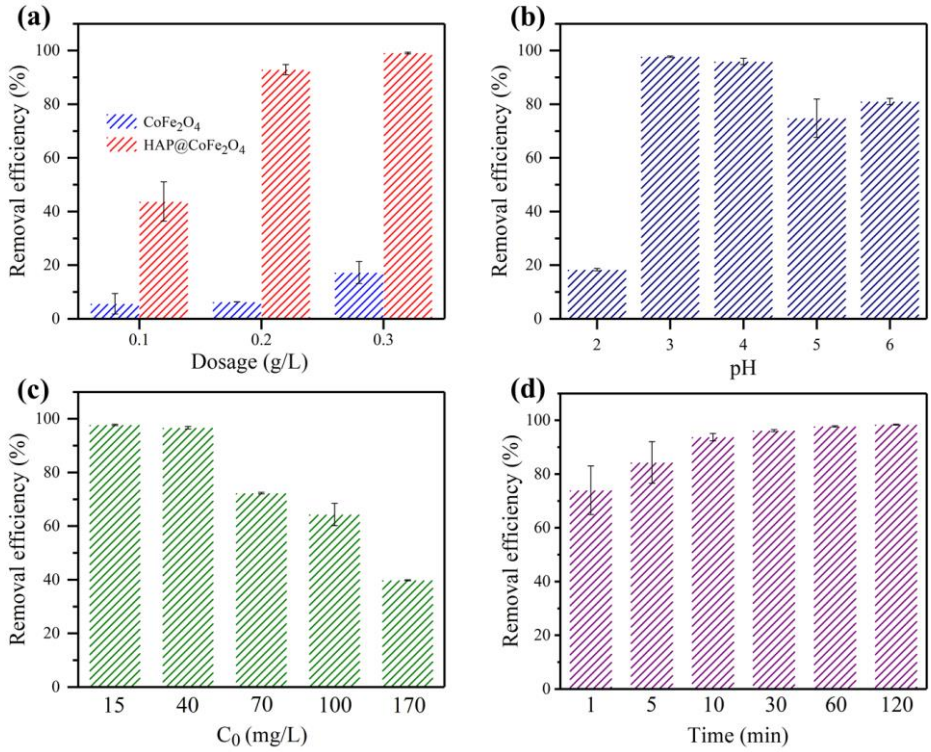

Figure 2. (**a**) Effect of dosage on the U(VI) adsorption of $CoFe_2O_4$ and HAP@$CoFe_2O_4$ at various dosages (Reaction conditions: initial U(VI) concentration = approximately 15 mg/L, pH = 3.0, adsorbent dosage = 0.1–0.3 g/L, T = 298 K); (**b**) Removal rate of U(VI) by magnetic HAP@$CoFe_2O_4$ under various pH (Reaction conditions: initial U(VI) concentration = approximately 15 mg/L, pH = 2.0–6.0, adsorbent dosage = 0.2 g/L, T = 298 K); (**c**) Effect of initial U(VI) concentration (reaction conditions: initial U(VI) concentration = 15–170 mg/L, pH = 3.0, adsorbent dosage = 0.2 g/L, T = 298 K); (**d**) Effect of contact time (reaction conditions: initial U(VI) concentration = approximately 15 mg/L, t = 0–120 min, pH = 3.0, adsorbent dosage = 0.2 g/L, T = 298 K).

Because pH is a critical factor affecting the interaction between HAP@$CoFe_2O_4$ particles and U(VI), experiments were performed to investigate the effect of the solution pH on U(VI) adsorption by changing the pH value (2.0–6.0) of the solution (Figure 2b). When the pH value was less than 3.0, U(VI) was mainly present in the form of uranyl ions (UO_2^{2+}) in the solution [47]. Moreover, HAP@$CoFe_2O_4$ is not stable under the conditions with a pH below 3.0 because the HAP might dissolve. A higher pH reduced protonation in the solution, and the U(VI) changed. At a low pH, the high H^+ concentration of the solution competed intensely with the UO_2^{2+}, which limited the UO_2^{2+} adsorption by the HAP@$CoFe_2O_4$. At pH = 3.0, the adsorption capacity considerably increased and reached the maximum. As the pH increased, the adsorption of U(VI) by HAP@$CoFe_2O_4$ weakened marginally. When the pH was 3.0 or higher, the charge of as-fabricated HAP@$CoFe_2O_4$ composite decreased and became negative [19]. Meanwhile, under high pH conditions, the UO_2^{2+} began to hydrolyze and form new species, such as $(UO_2)_2(OH)_2^{2+}$, $(UO_2)_3(OH)^{5+}$, $(UO_2)_4(OH)^{7+}$, $UO_2(OH)^+$, and $(UO_2)_3(OH)^{7-}$. The affinity of these species is generally lower than that of the UO_2^{2+} [48]. Therefore, the HAP@$CoFe_2O_4$ composite does not easily absorb these species. Nevertheless, the HAP@$CoFe_2O_4$ particles still maintained high adsorption of U(VI), which indicated that the composite material could efficiently adsorb U(VI) in a wide pH range, making it capable of removing uranium from contaminated wastewater under various conditions.

The reaction system comprising 0.2 g/L of sorbent and approximately 15 mg/L U(VI) exhibited the highest removal efficiency (Figure 2c). Figure 2d indicated that the adsorption efficiency of the HAP@$CoFe_2O_4$ was as high as 93% in 10 min. Initially, sufficient active surface sites were present, which resulted in a high adsorption efficiency and intensive interaction between the HAP@$CoFe_2O_4$ and U(VI). On prolonging the contact time, U(VI) ions occupied most of the active sites of the HAP@$CoFe_2O_4$, and the adsorption reached equilibrium at 30 min. Even when the time was increased, stable adsorption efficiency was maintained.

3.3. Adsorption Isotherms and Kinetics

To investigate the adsorption behavior, Langmuir (Equation (S2)) and Freundlich (Equation (S3)) isotherm models were used to simulate the adsorption process of the HAP@$CoFe_2O_4$ for U(VI). The correlation coefficients (R^2) of the HAP@$CoFe_2O_4$ were 0.9390 and 0.8663 for the Langmuir and Freundlich isotherm models, respectively (Figure 3a and Table 1). This result indicated that the adsorption process of U(VI) onto HAP@$CoFe_2O_4$ could be better interpreted using the Langmuir isotherm model than the Freundlich isotherm. On the basis of the Langmuir isotherm model, the Q_{max} of the HAP@$CoFe_2O_4$ for U(VI) was 338 mg/g, which was almost consistent with the experimental results. The two lower correlation coefficients may be due to the combined effects of physical adsorption and surface precipitation. In the process of the HAP@$CoFe_2O_4$ absorbing uranium, the dominant adsorption mechanism is related to the initial uranium concentration. Surface adsorption may contribute considerably to the total uranium adsorption at low uranium concentrations [49].

Table 1. Freundlich and Langmuir isotherm constants for the U(VI) adsorption onto the as-fabricated HAP@$CoFe_2O_4$ composite.

Materials	Langmuir Isotherm			Freundlich Isotherm		
	q_m(mg/g)	K_L(L/mg)	R^2	K_F(L/mg)	1/*n*	R^2
HAP@$CoFe_2O_4$	338	0.91	0.9981	145.64	0.20	0.8465

The fitting constants for pseudo-first-order (Equation (S4)) and pseudo-second-order (Equation (S5)) kinetic models are displayed in Figure 3b and Table 2. The pseudo-second-order kinetic model exhibited greater R^2 (0.9922) than that of the pseudo-first-order kinetic model (0.9790), which indicated that the kinetic process of the HAP@$CoFe_2O_4$ for U(VI)

was well described by the pseudo-second-order kinetic model. Furthermore, the adsorption capacity (67.61 mg/g) calculated using the pseudo-second-order kinetic model was consistent with the experimental result (68.85 mg/g), which indicated that the adsorption process of U(VI) by the HAP@$CoFe_2O_4$ was controlled by chemical adsorption.

Table 2. Kinetic parameters for the adsorption of U(VI) onto HAP@$CoFe_2O_4$.

Kinetics Model	Parameter	Values
Pseudo-first-order	k_1 (L mg^{-1})	1.539
	R^2	0.9790
	q_e	65.83
Pseudo-second-order	k_2 (L mg^{-1})	0.44
	R^2	0.9922
	q_e	67.61

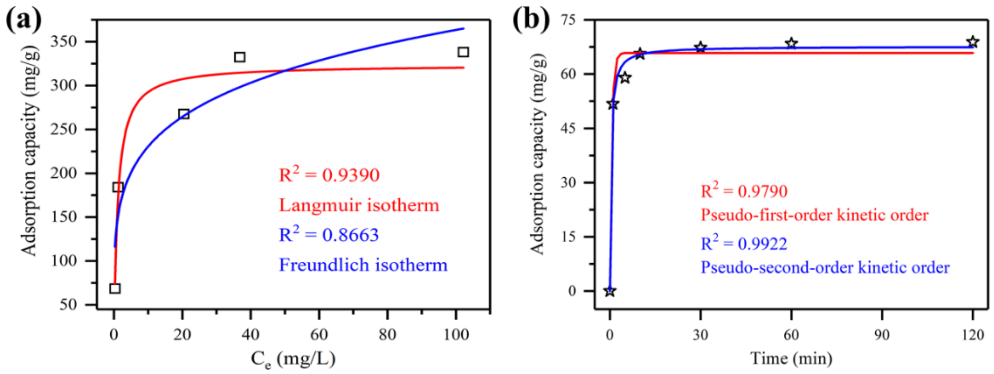

Figure 3. Isotherms and kinetics of U(VI) adsorption onto the as-fabricated HAP@$CoFe_2O_4$ composite: (**a**) Langmuir isotherm and Freundlich isotherm models, (**b**) pseudo-first-order and pseudo-second-order kinetics.

3.4. U(VI) Removal Mechanisms

XRD, FT-IR, and XPS were performed to understand the adsorption mechanism of U(VI) by the HAP@$CoFe_2O_4$ composite. The XRD patterns (Figure 4a) revealed that a uranium-containing compound was formed. After adsorption, numerous diffraction peaks were observed at 2θ = 10.523°, 18.009°, 20.903°, 24.738°, 25.576°, 27.724°, 35.880°, 40.972°, and 44.581°, which corresponded to the crystal planes of (001), (110), (111), (102), (200), (201), (212), (310), and (302) of the meta-autunite 9A [$(Ca(UO_2)_2(PO_4)_2(H_2O)_6$, PDF no. 72-2117]. These results were in good agreement with the standard pattern of autunite, which could be explained by the dissolution of the HAP and then precipitation of the autunite on the surface of the HAP [50]. The presence of autunite indicated a successful fixation of uranium on the adsorbent. The XRD pattern also illustrated the presence of $CoFe_2O_4$ in the adsorbed material, which proved that the adsorbent was still magnetic after the reaction.

FT-IR analysis (Figure 4b) revealed that both the adsorbents before and after the reaction exhibited a distinct single and wide peak at approximately 3445 cm^{-1}, which was attributed to the –OH groups. This result indicated that the existence of –OH groups in the HAP@$CoFe_2O_4$ is a typical feature of HAP [51]. The peak at 1616 cm^{-1} is characteristic of –COO, which could be attributed to the absorption of CO_2 in air during the test [40,41]. The peaks at 1044.82 and 602.94 cm^{-1}, (before adsorption) and 1007.83 and 600.90 cm^{-1} (after adsorption) were attributable to the PO_4^{3-} group in the adsorbent [40,52], and the position and intensity of the characteristic peaks in the adsorbent changed considerably before and after the reaction. The results revealed that the PO_4^{3-} in the HAP@$CoFe_2O_4$ is involved in the reaction. After the adsorption reaction, a new peak appeared at 546.327 cm^{-1}, which corresponded to Co/Fe–O bonding [53,54]. A new

absorption peak of the HAP@$CoFe_2O_4$ after the reaction appeared at 911 cm^{-1}, which was characteristic of UO_2^{2+}, providing strong evidence of uranium loading. The essence of removing U(VI) by using the HAP@$CoFe_2O_4$ is the chemical reaction between UO_2^{2+} and the HAP. The UO_2^{2+} was adsorbed and eventually incorporated into the Ca^{2+}–PO_4^{3-}–OH according to Equation (2):

$$Ca^{2+} + 2PO_4^{3-} + H_2O + 2UO_2^{2+} \rightarrow Ca(UO_2)_2(PO_4)_2(H_2O)_6 \quad (2)$$

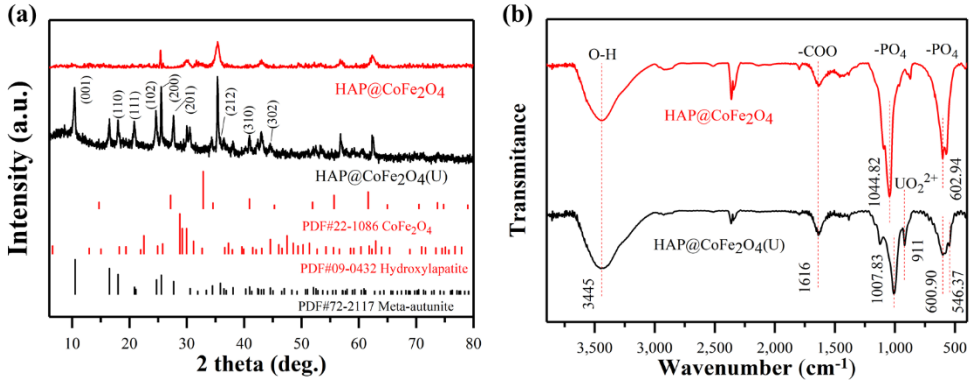

Figure 4. X-ray diffraction patterns (**a**) and FT-IR spectrum (**b**) of HAP@$CoFe_2O_4$ and U(VI)-loaded HAP@$CoFe_2O_4$.

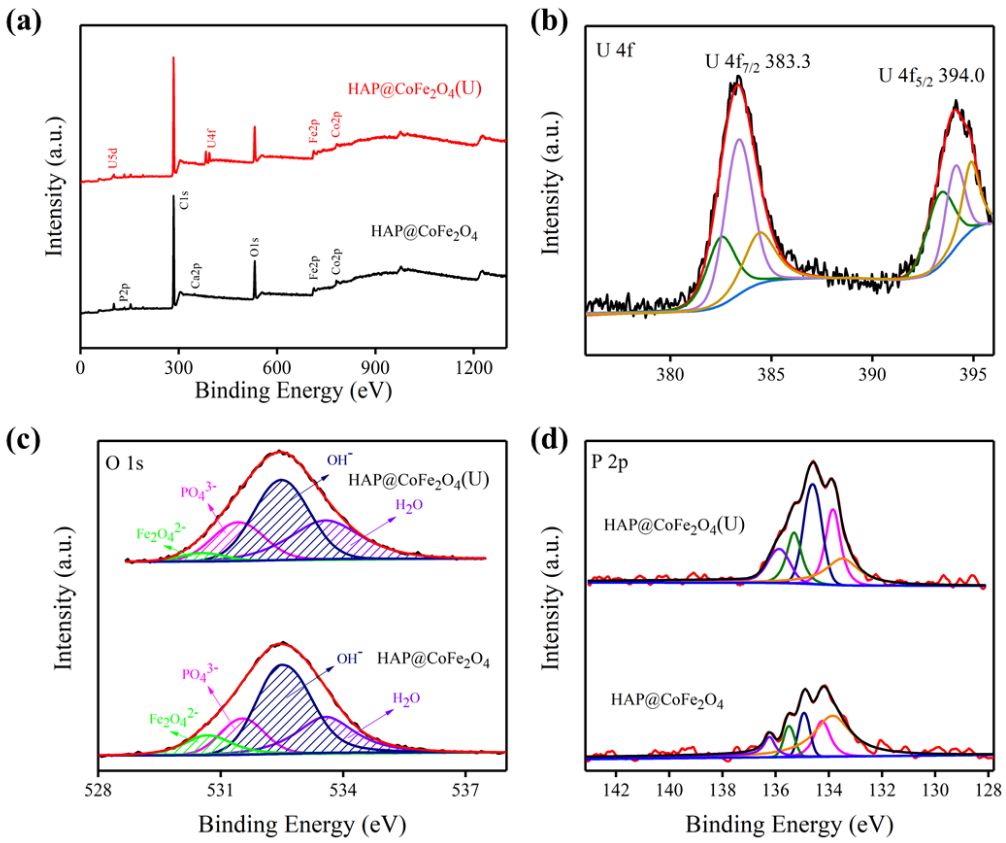

Figure 5. X-ray spectroscopy (XPS) full-survey spectra (**a**) as well as the (**b**) U 4f, (**c**) O 1s, (**d**) P 2p.

The XPS survey spectra (Figure 5a) revealed the peaks of C 1s, O 1s, Ca 2p, P 2p, Fe 2p, and Co 2p, which indicated that the $CoFe_2O_4$ was successfully loaded on the HAP. A new strong double peak for the antisymmetric vibration of $[O=UVI=O]^{2+}$ appeared in the XPS spectra of the HAP@$CoFe_2O_4$ reacted with U(VI), which was consistent with the EDS

elemental mapping results (Figure S1), suggesting that uranium was successfully adsorbed on the surface of the material. The high resolution of the U 4f spectrum (Figure 5b) can be well fitted at binding energies of 383.3 (U $4f_{7/2}$) and 394.0 eV (U $4f_{5/2}$), indicating that the valence of uranium did not change during the adsorption process [55,56]. The Co spectrum (Figure S2a) revealed two peaks at binding energies 782.58 and 786.84 eV, which were attributed to Co $2p_{3/2}$ and its shake-up satellites, respectively, whereas peaks at higher binding energies (~797.81 and 804.44 eV) corresponded to Co $2p_{1/2}$ and their shake-up satellites, respectively [57]. The Fe 2p spectrum (Figure S2b) displayed into two peaks at binding energies of 712.13 and 726.02 eV, which respectively correspond to Fe $2p_{3/2}$ and Fe $2p_{1/2}$, evidencing the existence of Fe^{3+} [58–60]. As displayed in Figure 5d, after reaction with U(VI), the P 2p peaks shifted slightly towards higher binding energy, which indicated that the presence of phosphorus considerably affected the adsorption of uranium [19]. The spectra of O 1s (Figure 5c) can be divided into four peaks, namely, anion oxide (530.64 eV, $Fe_2O_4^{2-}$), phosphate group (531.53 eV, PO_4^{3-}), hydroxyl groups (532.50 eV, −OH), and adsorbed groups (H_2O, 533.57 eV), respectively. The peak area ratio of –OH varied considerably (from 50.33% to 40.26%) before and after U(VI) adsorption, which evidenced that the surface hydroxyl groups (–OH) played a key role in the adsorption of U(VI) through the sharing of electrons to form U–O bonds [61,62].

3.5. Preliminary Evaluation of the U(VI) Removal Process

The suggested schematic of the removal of the U(VI) from wastewater using HAP@$CoFe_2O_4$ is presented in Figure 6, 93.7%, where the U(VI) was removed within 10 min. As a magnetic separable material, the advantage of using HAP@$CoFe_2O_4$ is that the adsorption/separation is a simple and efficient process, U(VI) can be effectively removed from wastewater and the U(VI) loaded can be easily separated from water using magnetic field, which is beneficial for the minimization of secondary waste. The process using HAP@$CoFe_2O_4$ as an adsorbent for the removal of U(VI) has economic feasibility. The use of HAP@$CoFe_2O_4$ for the U(VI) removal/separation could result in a significant reduction of costs due to easier separation of the solid phase and energy savings. HAP@$CoFe_2O_4$ can be considered to be an effective and environmental material for the elimination of U(VI) from mining wastewater.

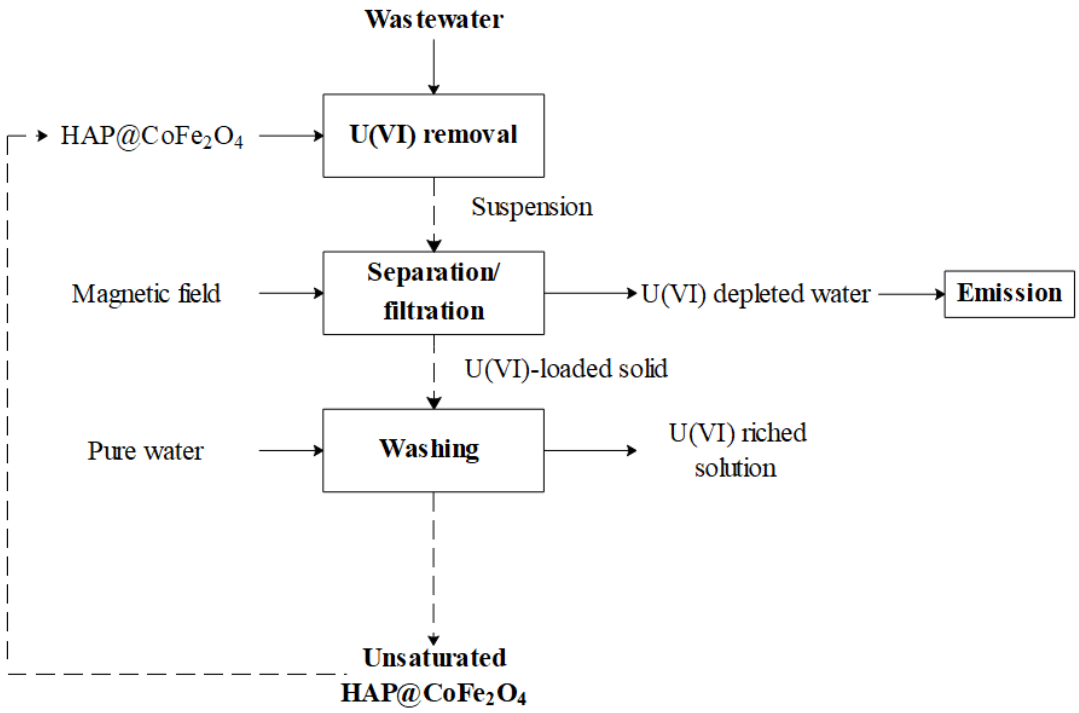

Figure 6. Schematic of the removal of U(VI) using HAP@$CoFe_2O_4$. The dashed lines present the solid phases.

4. Conclusions

This study developed a promising and easily separable composite material, HAP@$CoFe_2O_4$, for removing uranium ions from radioactive wastewater. A U(VI) removal efficiency of 93.7% can be achieved by the HAP@$CoFe_2O_4$ in 10 min, and the maximum adsorption capacity was 338 mg/g. Therefore, HAP@$CoFe_2O_4$ can be used as an emergency material to treat uranium-containing radioactive wastewater generated in nuclear accidents. The UO_2^{2+} were transferred to the HAP@$CoFe_2O_4$ by reacting with dissolved calcium and phosphate, thereby forming a more stable compound-autunite [$Ca(UO_2)_2(PO_4)_2(H_2O)_6$]. The adsorption and incorporation are the main ways for U(VI) removal. Simulation of the interaction process between the HAP@$CoFe_2O_4$ and UO_2^{2+} by using adsorption isotherm models and adsorption kinetic models revealed that the adsorption process followed the Langmuir isotherm and pseudo-second-order dynamic model, which indicated that the adsorption of U(VI) by the HAP@$CoFe_2O_4$ was mainly controlled by chemical adsorption. Moreover, the magnetic property of the as-prepared HAP@$CoFe_2O_4$ was measured and found to be used for magnetic separation. Therefore, the developed process using HAP@$CoFe_2O_4$ as an adsorbent is promising to mitigate uranium pollution generated in a nuclear accident, and a pilot scale test for process optimization is planned in the future.

Supplementary Materials: The following are available online at https://www.mdpi.com/article/10.3390/pr9111927/s1, Figure S1: EDS image of U(VI) loaded HAP@$CoFe_2O_4$. Figure S2: (a) Co 2p, and (b) Fe 2p XPS spectra of the HAP@$CoFe_2O_4$ composite before and after the removal of U(VI).

Author Contributions: Conceptualization, T.O. and Q.S.; Methodology, T.O. and Q.S.; Writing-Original Draft, T.O. and H.P.; Resources, M.S. and D.C.; Funding acquisition, M.S., N.C. and D.C.; Formal analysis, T.O. and J.T.; Writing—Review & Editing, T.O., M.S. and J.T.; Supervision, M.S. and D.C. All authors have read and agreed to the published version of the manuscript.

Funding: This research was funded by the National Natural Science Foundation of China (22076034, 41877290), the Natural Science Foundation of Guangdong Province of China (2021A1515010067) and Foundation of Department of Education of Guangdong Province of China (2018KTSCX176) and Guangzhou University Intramural Scientific Research Project (YG2020012).

Institutional Review Board Statement: Not applicable.

Informed Consent Statement: Not applicable.

Data Availability Statement: The data presented in this study are available in this article.

Acknowledgments: This work was supported by the National Natural Science Foundation of China (22076034, 41877290), the Natural Science Foundation of Guangdong Province of China (2021A1515010067), and Foundation of Department of Education of Guangdong Province of China (2018KTSCX176) and Guangzhou University Intramural Scientific Research Project (YG2020012).

Conflicts of Interest: The authors declare no conflict of interest.

References

1. Yang, Y.; Saiers, J.E.; Barnett, M.O. Impact of interactions between natural organic matter and metal oxides on the desorption kinetics of uranium from heterogeneous colloidal suspensions. *Environ. Sci. Technol.* **2013**, *47*, 2661–2669. [CrossRef]
2. Lu, S.H.; Zhu, K.R.; Hayat, T.; Alharbi, N.S.; Chen, C.L.; Song, G.; Chen, D.Y.; Sun, Y.B. Influence of carbonate on sequestration of U(VI) on perovskite. *J. Hazard. Mater.* **2019**, *364*, 100–107. [CrossRef]
3. Pan, Q.J.; Odoh, S.O.; Asaduzzaman, A.M.; Schreckenbach, G. Adsorption of uranyl species onto the rutile (110) surface: A periodic DFT study. *Chemistry* **2012**, *18*, 1458–1466. [CrossRef] [PubMed]
4. Kong, L.J.; Zhang, H.M.; Ji, W.; Shih, K.M.; Su, M.H.; Diao, Z.H.; Xu, R.M.; Hou, L.A.; Song, G.; Chen, D.Y. Recovery of phosphorus rich krill shell biowaste for uranium immobilization: A study of sorption behavior, surface reaction, and phase transformation. *Environ. Pollut.* **2018**, *243*, 630–636. [CrossRef] [PubMed]
5. Niu, Z.W.; Wei, X.Y.; Qiang, S.R.; Wu, H.Y.; Pan, D.Q.; Wu, W.S.; Fan, Q.H. Spectroscopic studies on U(VI) incorporation into $CaCO_3$: Effects of aging time and U(VI) concentration. *Chemosphere* **2019**, *220*, 1100–1107. [CrossRef] [PubMed]
6. Tang, J.F.; Su, M.H.; Wu, Q.H.; Wei, L.Z.; Wang, N.N.; Xiao, E.Z.; Zhang, H.G.; Wei, Y.J.; Liu, Y.K.; Ekberg, C.; et al. Highly efficient recovery and clean-up of four heavy metals from MSWI fly ash by integrating leaching, selective extraction and adsorption. *J. Clean. Prod.* **2019**, *234*, 139–149. [CrossRef]

7. Wang, D.; Xu, Y.B.; Xiao, D.F.; Qiao, Q.G.; Yin, P.; Yang, Z.L.; Li, J.X.; Winchester, W.; Wang, Z.; Hayat, T. Ultra-thin iron phosphate nanosheets for high efficient U(VI) adsorption. *J. Hazard. Mater.* **2019**, *371*, 83–93. [CrossRef]
8. Li, X.; Liu, Y.; Zhang, C.L.; Wen, T.; Zhuang, L.; Wang, X.X.; Song, G.; Chen, D.Y.; Ai, Y.J.; Hayat, T.; et al. Porous Fe_2O_3 microcubes derived from metal organic frameworks for efficient elimination of organic pollutants and heavy metal ions. *Chem. Eng. J.* **2018**, *336*, 241–252. [CrossRef]
9. Xia, X.; Shen, J.; Cao, F.; Wang, C.J.; Tang, M.; Zhang, Q.Y.; Wei, S.S. A facile synthesis of hydroxyapatite for effective removal strontium ion. *J. Hazard. Mater.* **2019**, *368*, 326–335. [CrossRef]
10. Liu, X.; Huang, Y.; Duan, S.; Wang, Y.; Li, J.; Chen, Y.; Hayat, T.; Wang, X. Graphene oxides with different oxidation degrees for Co(II) ion pollution management. *Chem. Eng. J.* **2016**, *302*, 763–772. [CrossRef]
11. Zhang, H.M.; Ruan, Y.; Liang, A.P.; Shih, K.M.; Diao, Z.H.; Su, M.H.; Hou, L.A.; Chen, D.Y.; Lu, H.; Kong, L.J. Carbothermal reduction for preparing nZVI/BC to extract uranium: Insight into the iron species dependent uranium adsorption behavior. *J. Clean. Prod.* **2019**, *239*, 117873. [CrossRef]
12. Wu, W.Y.; Chen, D.Y.; Li, J.W.; Su, M.H.; Chen, N. Enhanced adsorption of uranium by modified red muds: Adsorption behavior study. *Environ. Sci. Pollut. Res.* **2018**, *25*, 18096–18108. [CrossRef]
13. Su, M.H.; Liao, C.Z.; Chan, T.S.; Shih, K.M.; Xiao, T.F.; Chen, D.Y.; Kong, L.J.; Song, G. Incorporation of cadmium and nickel into ferrite spinel solid solution: X-ray diffraction and X-ray absorption fine structure analyses. *Environ. Sci. Technol.* **2018**, *52*, 775–782. [CrossRef] [PubMed]
14. Wu, H.Y.; Li, P.; Pan, D.Q.; Yin, Z.X.; Fang, Q.H.; Wu, W.S. Interactions between silicon oxide nanoparticles (SONPs) and U(VI) contaminations: Effects of pH, temperature and natural organic matters. *Plos One* **2016**, *11*, e0149632. [CrossRef] [PubMed]
15. Li, D.E.; Kaplan, D.I.; Chang, H.S.; Seaman, J.C.; Jaffe, P.R.; van Groos, P.K.; Scheckel, K.G.; Segre, C.U.; Chen, N.; Jiang, D.T.; et al. Spectroscopic evidence of uranium immobilization in acidic wetlands by natural organic matter and plant roots. *Environ. Sci. Technol.* **2015**, *49*, 2823–2832. [CrossRef] [PubMed]
16. Yuvaraja, G.; Su, M.; Chen, D.Y.; Pang, Y.; Kong, L.J.; Subbaiah, M.V.; Wen, J.C.; Reddy, G.M. Impregnation of magnetic—Momordica charantia leaf powder into chitosan for the removal of U(VI) from aqueous and polluted wastewater. *Int. J. Biol. Macromol.* **2020**, *149*, 127–139. [CrossRef]
17. Krajňák, A.; Viglašová, E.; Galamboš, M.; Krivosudský, L. Application of HDTMA-intercalated bentonites in water waste treatment for U(VI) removal. *J. Radioanal. Nucl. Chem.* **2017**, *314*, 2489–2499. [CrossRef]
18. Wen, H.; Pan, Z.Z.; Giammar, D.; Li, L. Enhanced uranium immobilization by phosphate amendment under variable geochemical and flow conditions: Insights from reactive transport modeling. *Environ. Sci. Technol.* **2018**, *52*, 5841–5850. [CrossRef] [PubMed]
19. Zheng, N.C.; Yin, L.Y.; Su, M.H.; Liu, Z.Q.; Tsang, D.C.W.; Chen, D.Y. Synthesis of shape and structure-dependent hydroxyapatite nanostructures as a superior adsorbent for removal of U(VI). *Chem. Eng. J.* **2020**, *384*, 123262. [CrossRef]
20. Kong, L.J.; Ruan, Y.; Zheng, Q.Y.; Su, M.H.; Diao, Z.H.; Chen, D.Y.; Hou, L.A.; Chang, X.Y.; Shih, K.M. Uranium extraction using hydroxyapatite recovered from phosphorus containing wastewater. *J. Hazard. Mater.* **2020**, *382*, 120784. [CrossRef]
21. Chen, B.D.; Wang, J.; Kong, L.J.; Mai, X.X.; Zheng, N.C.; Zhong, Q.H.; Liang, J.Y.; Chen, D.Y. Adsorption of uranium from uranium mine contaminated water using phosphate rock apatite (PRA): Isotherm, kinetic and characterization studies. *Colloids Surf. A* **2017**, *520*, 612–621. [CrossRef]
22. Cumberland, S.A.; Douglas, G.; Grice, K.; Moreau, J.W. Uranium mobility in organic matter-rich sediments: A review of geological and geochemical processes. *Earth-Sci. Rev.* **2016**, *159*, 160–185. [CrossRef]
23. Burns, P.C. U^{6+} minerals and inorganic compounds: Insights into an expanded structural hierarchy of crystal structures. *Can. Mineral.* **2005**, *43*, 1839–1894. [CrossRef]
24. Zhou, Y.; Li, W.; Jiang, X.; Sun, Y.; Yang, H.; Liu, Q.; Cao, Y.; Zhang, Y.; Cheng, H. Synthesis of strontium (Sr) doped hydroxyapatite (HAp) nanorods for enhanced adsorption of Cr (VI) ions from wastewater. *Ceram. Int.* **2021**, *47*, 16730–16736. [CrossRef]
25. Ma, J.; Xia, M.; Zhu, S.; Wang, F. A new alendronate doped HAP nanomaterial for Pb^{2+}, Cu^{2+} and Cd^{2+} effect absorption. *J. Hazard. Mater.* **2020**, *400*, 123143. [CrossRef]
26. Xiong, T.; Li, Q.; Liao, J.; Zhang, Y.; Zhu, W. Highly enhanced adsorption performance to uranium(VI) by facile synthesized hydroxyapatite aerogel. *J. Hazard. Mater.* **2022**, *423*, 127184. [CrossRef] [PubMed]
27. Su, M.H.; Tsang, D.C.W.; Ren, X.Y.; Shi, Q.P.; Tang, J.F.; Zhang, H.G.; Kong, L.J.; Hou, L.A.; Song, G.; Chen, D.Y. Removal of U(VI) from nuclear mining effluent by porous hydroxyapatite: Evaluation on characteristics, mechanisms and performance. *Environ. Pollut.* **2019**, *254*, 112891. [CrossRef]
28. Ghaffarian, F.; Ghasemzadeh, M.A.; Aghaei, S.S. An efficient synthesis of some new curcumin based pyrano[2,3-d] pyrimidine-2,4(3H)-dione derivatives using $CoFe_2O_4$@OCMC@Cu(BDC) as a novel and recoverable catalyst. *J. Mol. Struct.* **2019**, *1186*, 204–211. [CrossRef]
29. Dey, C.; Baishya, K.; Ghosh, A.; Goswami, M.M.; Ghosh, A.; Mandal, K. Improvement of drug delivery by hyperthermia treatment using magnetic cubic cobalt ferrite nanoparticles. *J. Magn. Magn. Mater.* **2017**, *427*, 168–174. [CrossRef]
30. Tartaj, P.; Morales, M.D.; Veintemillas-Verdaguer, S.; Gonzalez-Carreno, T.; Serna, C.J. The preparation of magnetic nanoparticles for applications in biomedicine. *J. Phys. D: Appl. Phys.* **2003**, *36*, R182–R197. [CrossRef]
31. Chandra, G.; Srivastava, R.C.; Reddy, V.R.; Agrawal, H.M. Effect of sintering temperature on magnetization and Mossbauer parameters of cobalt ferrite nanoparticles. *J. Magn. Magn. Mater.* **2017**, *427*, 225–229. [CrossRef]

32. Zhu, H.; Shen, Y.; Wang, Q.; Chen, K.; Wang, X.; Zhang, G.; Yang, J.; Guo, Y.; Bai, R. Highly promoted removal of Hg(II) with magnetic $CoFe_2O_4$@SiO_2 core–shell nanoparticles modified by thiol groups. *RSC Adv.* **2017**, *7*, 39204–39215. [CrossRef]
33. Coutinho, T.C.; Malafatti, J.O.D.; Paris, E.C.; Tardioli, P.W.; Farinas, C.S. Hydroxyapatite-$CoFe_2O_4$ magnetic nanoparticle composites for industrial enzyme immobilization, use, and recovery. *ACS Appl. Nano Mater.* **2020**, *3*, 12334–12345. [CrossRef]
34. Ansari, S.M.; Ghosh, K.C.; Devan, R.S.; Sen, D.; Sastry, P.U.; Kolekar, Y.D.; Ramana, C.V. Eco-friendly synthesis, crystal chemistry, and magnetic properties of manganese-substituted $CoFe_2O_4$ nanoparticles. *ACS Omega* **2020**, *5*, 19315–19330. [CrossRef] [PubMed]
35. Cao, Z.; Zuo, C. Direct synthesis of magnetic $CoFe_2O_4$ nanoparticles as recyclable photo-fenton catalysts for removing organic dyes. *ACS Omega* **2020**, *5*, 22614–22620. [CrossRef] [PubMed]
36. Dos Santos, J.M.N.; Pereira, C.R.; Pinto, L.A.A.; Frantz, T.; Lima, E.C.; Foletto, E.L.; Dotto, G.L. Synthesis of a novel $CoFe_2O_4$/chitosan magnetic composite for fast adsorption of indigotine blue dye. *Carbohyd. Polym.* **2019**, *217*, 6–14. [CrossRef]
37. Foroughi, F.; Hassanzadeh-Tabrizi, S.A.; Amighian, J.; Saffar-Teluri, A. A designed magnetic $CoFe_2O_4$–hydroxyapatite core–shell nanocomposite for Zn(II) removal with high efficiency. *Ceram. Int.* **2015**, *41*, 6844–6850. [CrossRef]
38. Elizalde, M.L.M.; Acha, C.; Molina, F.V.; Antonel, P.S. Composites of poly(3,4-ethylenedioxythiophene) and $CoFe_2O_4$ nanoparticles: Composition influence on structural, electrical, and magnetic properties. *J. Phys. Chem. C* **2020**, *124*, 6884–6895. [CrossRef]
39. Manikandan, V.; Mirzaei, A.; Vigneselvan, S.; Kavita, S.; Mane, R.S.; Kim, S.S.; Chandrasekaran, J. Role of ruthenium in the dielectric, magnetic properties of nickel ferrite (Ru-$NiFe_2O_4$) nanoparticles and their application in hydrogen sensors. *ACS Omega* **2019**, *4*, 12919–12926. [CrossRef]
40. Shi, Q.P.; Su, M.H.; Yuvaraja, G.; Tang, J.F.; Kong, L.J.; Chen, D.Y. Development of highly efficient bundle-like hydroxyapatite towards abatement of aqueous U(VI) ions: Mechanism and economic assessment. *J. Hazard. Mater.* **2020**, *394*, 122550. [CrossRef] [PubMed]
41. Champeau, M.; Thomassin, J.M.; Jerome, C.; Tassaing, T. In situ FT-IR micro-spectroscopy to investigate polymeric fibers under supercritical carbon dioxide: CO2 sorption and swelling measurements. *J. Supercrit. Fluids* **2014**, *90*, 44–52. [CrossRef]
42. Tsuru, K.; Yoshimoto, A.; Kanazawa, M.; Sugiura, Y.; Nakashima, Y.; Ishikawa, K. Fabrication of carbonate apatite block through a dissolution–precipitation reaction using calcium hydrogen phosphate dihydrate block as a precursor. *Materials* **2017**, *10*, 374. [CrossRef]
43. Tchoffo, R.; Ngassaa, G.B.P.; Tonlé, I.K.; Ngameni, E. Electroanalysis of diquat using a glassy carbon electrode modified with natural hydroxyapatite and β-cyclodextrin composite. *Talanta* **2021**, *222*, 121550. [CrossRef] [PubMed]
44. Crocella, V.; Cavani, F.; Cerrato, G.; Cocchi, S.; Comito, M.; Magnacca, G.; Morterra, C. On the role of morphology of $CoFeO_4$ spinel in methanol anaerobic oxidation. *J. Phys. Chem. C* **2012**, *116*, 14998–15009. [CrossRef]
45. Debnath, B.; Bansal, A.; Salunke, H.G.; Sadhu, A.; Bhattacharyya, S. Enhancement of magnetization through interface exchange interactions of confined NiO nanoparticles within the mesopores of $CoFe_2O_4$. *J. Phys. Chem. C* **2016**, *120*, 5523–5533. [CrossRef]
46. He, Q.M.; Rui, K.; Che, C.H.; Yang, J.H.; Wen, Z.Y. Interconnected $CoFe_2O_4$–polypyrrole nanotubes as anode materials for high performance sodium ion batteries. *Acs Appl. Mater. Inter.* **2017**, *9*, 36927–36935. [CrossRef] [PubMed]
47. Camacho, L.M.; Deng, S.G.; Parra, R.R. Uranium removal from groundwater by natural clinoptilolite zeolite: Effects of pH and initial feed concentration. *J. Hazard. Mater.* **2010**, *175*, 393–398. [CrossRef]
48. Li, X.L.; Wu, J.J.; Liao, J.L.; Zhang, D.; Yang, J.J.; Feng, Y.; Zeng, J.H.; Wen, W.; Yang, Y.Y.; Tang, J.; et al. Adsorption and desorption of uranium (VI) in aerated zone soil. *J. Environ. Radioact.* **2013**, *115*, 143–150. [CrossRef] [PubMed]
49. Guan, D.X.; Ren, C.; Wang, J.; Zhu, Y.; Zhu, Z.; Li, W. Characterization of lead uptake by nano-sized hydroxyapatite: A molecular scale perspective. *ACS Earth Space Chem.* **2018**, *2*, 599–607. [CrossRef]
50. Fuller, C.C.; Bargar, J.R.; Davis, J.A.; Piana, M.J. Mechanisms of uranium interactions with hydroxyapatite: Implications for groundwater remediation. *Environ. Sci. Technol.* **2002**, *36*, 158–165. [CrossRef]
51. Han, M.N.; Kong, L.J.; Hu, X.L.; Chen, D.Y.; Xiong, X.Y.; Zhang, H.M.; Su, M.H.; Diao, Z.H.; Ruan, Y. Phase migration and transformation of uranium in mineralized immobilization by wasted bio-hydroxyapatite. *J. Clean. Prod.* **2018**, *197*, 886–894. [CrossRef]
52. El-Maghrabi, H.H.; Younes, A.A.; Salem, A.R.; Rabie, K.; El-shereafy, E.-S. Magnetically modified hydroxyapatite nanoparticles for the removal of uranium (VI): Preparation, characterization and adsorption optimization. *J. Hazard. Mater.* **2019**, *378*, 120703. [CrossRef]
53. Teng, Y.; Liu, Z.Y.; Yao, K.; Song, W.B.; Sun, Y.J.; Wang, H.L.; Xu, H.H. Preparation of attapulgite/$CoFe_2O_4$ magnetic composites for efficient adsorption of tannic acid from aqueous solution. *Int. J. Environ. Res. Public Health* **2019**, *16*, 2187. [CrossRef]
54. Deng, L.; Shi, Z.; Peng, X.X. Adsorption of Cr(VI) onto a magnetic $CoFe_2O_4$/MgAl-LDH composite and mechanism study. *RSC Adv.* **2015**, *5*, 61. [CrossRef]
55. Guo, Y.; Gong, Z.; Li, C.; Gao, B.; Li, P.; Wang, X.; Zhang, B.; Li, X. Efficient removal of uranium (VI) by 3D hierarchical Mg/Fe-LDH supported nanoscale hydroxyapatite: A synthetic experimental and mechanism studies. *Chem. Eng. J.* **2020**, *392*, 123682. [CrossRef]
56. Feng, Y.; Ma, B.; Guo, X.; Sun, H.; Zhang, Y.; Gong, H. Preparation of amino-modified hydroxyapatite and its uranium adsorption properties. *J. Radioanal. Nucl. Chem.* **2018**, *319*, 437–446. [CrossRef]
57. Tan, L.C.; Liu, Q.; Jing, X.Y.; Liu, J.Y.; Song, D.L.; Hu, S.X.; Liu, L.H.; Wang, J. Removal of uranium(VI) ions from aqueous solution by magnetic cobalt ferrite/multiwalled carbon nanotubes composites. *Chem. Eng. J.* **2015**, *273*, 307–315. [CrossRef]

58. Zhou, L.C.; Ji, L.Q.; Ma, P.C.; Shao, Y.M.; Zhang, H.; Gao, W.J.; Li, Y.F. Development of carbon nanotubes/ $CoFe_2O_4$ magnetic hybrid material for removal of tetrabromobisphenol A and Pb(II). *J. Hazard. Mater.* **2014**, *265*, 104–114. [CrossRef]
59. Xiong, S.Q.; Ye, S.D.; Hu, X.H.; Xie, F.Z. Electrochemical detection of ultra-trace Cu(II) and interaction mechanism analysis between amine-groups functionalized $CoFe_2O_4$/reduced graphene oxide composites and metal ion. *Electrochim. Acta* **2016**, *217*, 24–33. [CrossRef]
60. Dong, Y.C.; Chui, Y.S.; Ma, R.G.; Cao, C.W.; Cheng, H.; Li, Y.Y.; Zapien, J.A. One-pot scalable synthesis of Cu-$CuFe_2O_4$/graphene composites as anode materials for lithium-ion batteries with enhanced lithium storage properties. *J. Mater. Chem. A* **2014**, *2*, 13892–13897. [CrossRef]
61. Chen, L.; Zhang, K.S.; He, J.Y.; Xu, W.H.; Huang, X.J.; Liu, J.H. Enhanced fluoride removal from water by sulfate-doped hydroxyapatite hierarchical hollow microspheres. *Chem.Eng. J.* **2016**, *285*, 616–624. [CrossRef]
62. Wu, F.C.; Pu, N.; Ye, G.; Sun, T.X.; Wang, Z.; Song, Y.; Wang, W.Q.; Huo, X.M.; Lu, Y.X.; Chen, J. Performance and mechanism of uranium adsorption from seawater to poly(dopamine)-inspired sorbents. *Environ. Sci. Technol.* **2017**, *51*, 4606–4614. [CrossRef] [PubMed]